



In₂O₃ nanoporous nanosphere: A highly efficient photocatalyst for decomposition of perfluorooctanoic acid

Zhenmin Li, Pengyi Zhang*, Tian Shao, Xiaoyun Li

State Key Joint Laboratory of Environment Simulation and Pollution Control, School of Environment, Tsinghua University, Beijing 100084, China

ARTICLE INFO

Article history:

Received 8 April 2012

Received in revised form 12 June 2012

Accepted 17 June 2012

Available online 23 June 2012

Keywords:

Indium oxide

Self-assembly

Nanoporous nanostructure

Perfluorooctanoic acid

Photocatalysis

ABSTRACT

Perfluorooctanoic acid (PFOA) is an emerging persistent organic pollutant and receives increasing concerns due to its global occurrence and resistance to most conventional decomposition methods. In₂O₃ nanoporous nanospheres (NPNs) with uniform size (~100 nm) were obtained by calcining nanoporous InOOH/In(OH)₃ nanospheres and its photocatalytic activity for PFOA decomposition were evaluated. The InOOH/In(OH)₃ precursor was self-assembled from ultrathin nanoplates (~2 nm) in an ethylenediamine-assisted alcohol-thermal system. The In₂O₃ NPNs possessed a high value of specific surface area (39.0 m² g⁻¹) and a large number of nanopores (~6 nm). Compared with commercial In₂O₃ nanocrystals (NCs) and TiO₂ (Degussa P25), In₂O₃ NPNs showed a remarkable photocatalytic activity to decompose PFOA with the half-life of 7.1 min. The first-order rate constant of PFOA by In₂O₃ NPNs was nearly 9 and 54.6 times higher than that by In₂O₃ NCs and TiO₂ respectively. The superior activity of In₂O₃ NPNs for PFOA decomposition can be attributed to its nanoporous structure, large specific surface area, and direct reaction between the photogenerated hole and PFOA.

© 2012 Elsevier B.V. All rights reserved.

1. Introduction

Perfluorooctanoic acid (PFOA, C₇F₁₅COOH) is a synthetic chemical compound that belongs to a class of fully fluorinated hydrocarbons known as perfluorocarboxylic acids (PFCAs, C_nF_{2n+1}COOH). PFCAs are widely used as industrial surfactants, additives, firefighting foams, and lubricants for their hydrophobic and lipophobic properties, and their high chemical and thermal stabilities. PFOA, as an emerging persistent organic pollutant, has increasingly attracted worldwide concerns in recent years due to its global occurrence in various environments and potential toxicity. PFOA has been ubiquitously detected in the blood of humans and animals such as fish, birds, and even the seals in the remote arctic regions [1–3]. Toxicological studies have demonstrated that exposure to PFOA can lead to developmental and reproductive toxicity, liver damage, and possibly cancer [4,5]. PFOA is bioaccumulative, recalcitrant, and resistant to natural decomposition and most conventional treatment processes [6–8]. Therefore, the development of PFOA decomposition technologies are much required.

Some special techniques such as ultrasonication [9,10], aqueous electron reduction [11], persulfate photolysis [12,13], and phosphotungstic-acid photocatalysis [14,15] have been developed to decompose PFOA. However, the existing methods are not satisfactory due to their harsh reaction conditions or/and high energy

consumption [16]. Heterogeneous photocatalysis based on TiO₂ is an effective mild method for the treatment of various organic contaminated waters. Although numerous organic pollutants including halogenated compounds can be readily photocatalyzed to CO₂ and H₂O by TiO₂, the treatment of PFOA with TiO₂ was only achieved with a limited success because of its very low catalytic activity and mineralization. A highly acidic condition (pH < 2) [17,18] or sonication assistance [19] is necessary to achieve PFOA decomposition by TiO₂ photocatalysis. Recently titanate nanotube [20] was used as photocatalyst to assist photodecomposition of PFOA, however the reaction rate is very low, and the titanate nanotube even delayed the direct photolysis of PFOA. Therefore, it is still a meaningful and challenging work to develop a highly efficient photocatalyst for decomposing PFOA.

In₂O₃ is an indirect band semiconductor with a direct band gap of 3.6 eV and an indirect band gap of 2.8 eV [21]. It is known as a transparent conducting oxide material and has been widely applied in solar cells, sensor modules, and transparent electrode materials for both electrochemical cells and liquid crystal display devices [22,23]. As a wide bandgap semiconductor, In₂O₃ has been applied to improve the photocatalytic efficiency of other semiconductors [24–26]. In₂O₃ and its composite oxides have also been investigated as water-splitting photocatalysts [27–29]. However, the photocatalytic ability of In₂O₃ for decomposition of PFCAs has not been examined.

Nanoporous materials have received a great deal of interest because of their wide applications in the fields of catalysis [30,31], environmental engineering [32], sensor systems [33] and

* Corresponding author. Tel.: +86 10 62796840; fax: +86 10 62797760.
E-mail address: zpy@tsinghua.edu.cn (P. Zhang).

so on. For photocatalysts with a nanoporous structure, recombination of photogenerated carriers (e^-/h^+) in the bulk is reduced and, moreover, a quicker surface e^-/h^+ separation, faster interfacial charge-carrier transfer, and better charge-carrier trapping are achieved [30]. Recently, Hu et al. [34] have demonstrated that the ZnS nanoporous nanospheres are more effective photocatalysts than Degussa P25 titania or ZnS nanocrystals in the photodegradation of eosin B at ambient temperature. Li et al. [35] reported that ZnS– In_2S_3 – In_2S_3 –CuS nanoporous nanospheres showed excellent photocatalytic activity for water splitting. These results demonstrate that nanoporous semiconductor nanospheres provide a new pathway to design and fabricate novel photocatalytic materials with high activity.

Alcohol-thermal synthesis by using ethanol as organic solvent has been used to prepare nanostructured materials at relatively low temperatures [36–38]. Compared with the hydrothermal synthesis, the crystallization rate is considerably slowed during the alcohol-thermal synthesis due to the inherently low polarity of ethanol solvent. Herein, we report synthesis of uniform In_2O_3 nanoporous nanospheres (NPNs) via an ethylenediamine-assisted alcohol-thermal method followed by calcination, in which ethylenediamine was used as an agent to modify and control the shape of nanostructures. The as-prepared In_2O_3 NPNs possess uniform size, high surface area, and more interestingly it exhibits remarkable photocatalytic activity for PFOA decomposition under mild conditions.

2. Experimental

2.1. Preparation of In_2O_3 NPNs

All reagents (purchased from Beijing Chemical Co., Ltd.) were analytical grade and were used as received. In_2O_3 NPNs were synthesized with a solvothermal method followed by calcination. In a typical preparation, 1.77 mmol of $\text{In}(\text{NO}_3)_3 \cdot 4.5\text{H}_2\text{O}$ (>99.5%) was dissolved in 34 mL of ethanol (>99.7%). Then 34 mL of ethylenediamine (>99.0%) was dropped into the above solution with continuous stirring. After stirred for 15 min, the mixture was transferred into a 100 mL Teflon-lined stainless steel autoclave. Then the autoclave was sealed and maintained at 180 °C for 16 h. After the autoclave was cooled down to room temperature naturally, the white precipitate (precursor) in the autoclave was collected by centrifugation, and washed with deionized water and ethanol for several times. In_2O_3 NPNs were obtained from the precursor via calcination at 500 °C for 2 h in air. To learn the time-dependent phase and morphology transformation of In_2O_3 precursor, other solvothermal time, i.e. 1 h, 3 h or 6 h, was selected to synthesize the corresponding precursors.

2.2. Characterization

X-ray powder diffraction (XRD) patterns were taken on a PANalytical X'Pert Pro diffractometer at 40 kV voltage and 30 mA current. The morphologies of the samples were observed by using an ultra high-resolution field-emission scanning electron microscope (FESEM, S-5500, Hitachi) performed at an accelerating voltage of 5.0 kV. Transmission electron microscopy (TEM) images and the corresponding selected area electron diffraction (SAED) patterns were taken on a JEM 2010F microscope at an accelerating voltage of 200 kV. The porosity and adsorption performance of the samples were determined via a Micromeritics ASAP-2000 nitrogen adsorption apparatus. The diffuse reflectance absorption spectra (DRS) of the samples were recorded on a UV–vis spectrophotometer (Hitachi UV-3100) equipped with an integrated sphere attachment. The electron spin resonance (ESR) signals of hydroxyl radicals (OH^\bullet) trapped by 5,5-dimethyl-1-pyrroline-N-oxide

(DMPO) (purchased from Sigma Chemical Co.) were examined on a JEOL JES FA-200 at ambient temperature under irradiation of a mercury lamp (ES-USH500, 500 W) with a filter (UV-D35, 270–440 nm for 76% transmission, >680 nm for 24% transmission).

2.3. Photocatalytic decomposition of PFOA

The photocatalytic decomposition of PFOA was conducted in a tubular quartz vessel reactor under UV irradiation. A low-pressure mercury lamp (23 W) emitting 254 nm UV light was placed in the center of the reactor with two-layer quartz tubes protection. A 0.05 g portion of In_2O_3 NPNs was suspended in 100 mL PFOA (Acros, 96%) aqueous solution ($C_0 = 30 \text{ mg L}^{-1}$) without extra addition of acid or alkali. Before irradiation, the suspensions were stirred in the dark for 1 h to ensure the establishment of adsorption–desorption equilibrium. Then, the suspension was poured into the tubular reactor. Oxygen gas was continuously bubbled into the reactor through a microporous glass plate at a flow rate of 60 mL min^{-1} during the whole reaction. Then the UV lamp was turned on and the reactions temperature was maintained constant with a cooling water jacket around the reactor. Commercial In_2O_3 nanocrystals (NCs) (Beijing Chemical Co. Ltd., >99.99%) and TiO_2 (Degussa P25) were adopted as the reference with which to compare the photocatalytic activity under the same experimental conditions.

2.4. Analyses

An ultra performance liquid chromatography–tandem mass spectrometry (UPLC–MS/MS) was used to determine the concentrations of PFOA. The UPLC system (Waters Corp., USA) was equipped with a C18 column (2.1 mm \times 50 mm i.d., particle size 1.7 μm , Waters Corp., USA). And the MS system was Quattro Premier XE tandem quadrupole mass spectrometer (Waters Corp., USA) with an electrospray ionization source. The mobile phase was a binary mixture of solvent A (2 mmol L^{-1} ammonium acetate in 100% methanol) and solvent B (2 mmol L^{-1} ammonium acetate in 5% methanol) at a flow rate of 0.3 mL min^{-1} . The gradient started with 25% A and 75% B, and linearly ramped to 85% A and 15% B in 5 min, and ramped to 25% A and 75% B in the following 2 min, then the column was allowed to equilibrate for 3 min, and the total running time was 10 min. The injection volume of samples was 10 μL . The tandem MS analysis was conducted in the multiple reaction monitoring (MRM) mode, and the cone voltage and collision energy were 30 V and 11 V, respectively. Other shorter-chain perfluorocarboxylic acids (PFCAs) including perfluoroheptanoic acid (PFHpA), perfluorohexanoic acid (PFHxA), perfluoropentanoic acid (PFPeA), perfluorobutanoic acid (PFBA) and trifluoroacetic acid (TFA) were also determined with the same method mentioned above. Aqueous standard solutions containing PFOA and C_2 – C_7 shorter-chain PFCAs were prepared to make external calibration curves in the range of 10–900 $\mu\text{g L}^{-1}$.

Concentrations of fluoride ion (F^-) were determined by ion chromatography (Metrohm 761 compact IC, Switzerland). Sample was injected into Metrosep A supp 5 column (150 mm length \times 4.0 mm i.d.) with a Metrosep R guard column. A mixture solution containing 3.2 mM Na_2CO_3 and 1 mM NaHCO_3 was used as the mobile phase and its flow rate was set at 1.0 mL min^{-1} . The limit of detection (LOD) was 0.01 mg L^{-1} .

Defluorination ratio was calculated as follows:

$$\text{Defluorination ratio} = \frac{C_{\text{F}^-}}{C_{\text{PFOA}} \times 15} \quad (1)$$

where C_{F^-} is concentration of fluoride ion (mM), C_{PFOA} is initial concentration of PFOA (mM), and the factor 15 corresponds to the number of fluorine atoms in PFOA molecule.

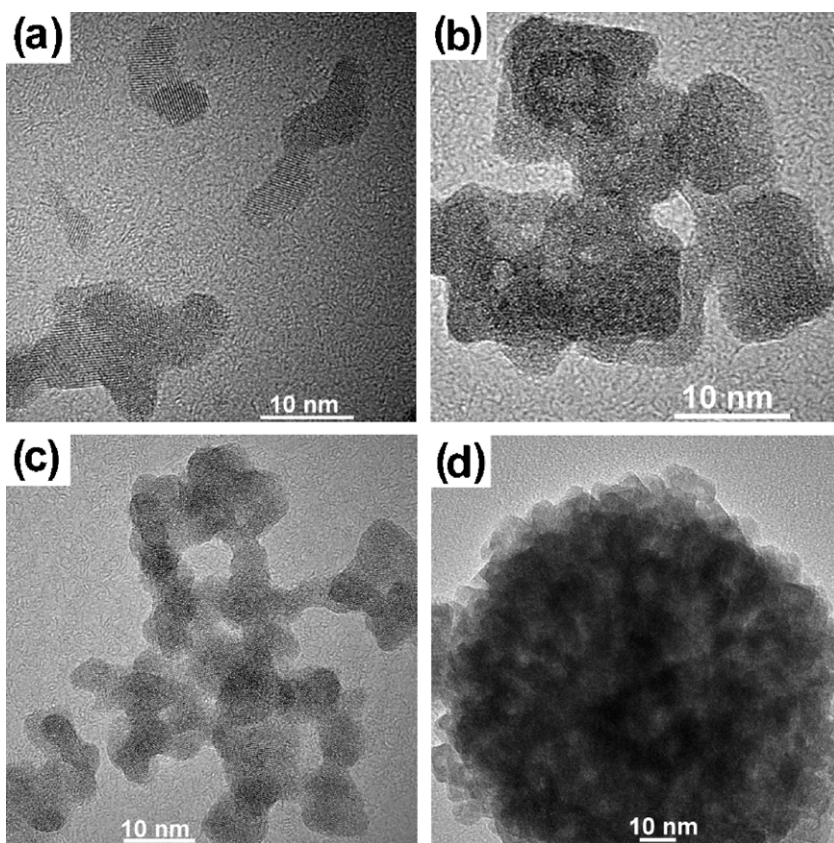


Fig. 1. TEM images of the products obtained after different solvothermal time: (a) 1 h, (b) 3 h, (c) 6 h, and (d) 16 h.

3. Results and discussion

3.1. Time-dependent phase and morphology transformation of In_2O_3 precursor

The In_2O_3 precursors were prepared by a solvothermal method with ethanol and ethylenediamine ($v/v = 1:1$) as solvents. To learn the formation process of In_2O_3 precursor and obtain nanomaterials with appropriate morphology, a detailed time-dependent morphology and phase study were conducted. The product obtained after solvothermal reaction for 1 h was composed of nanoplates with size of 5–10 nm (Fig. 1a), and its crystal phase was pure $\text{In}(\text{OH})_3$ (JCPDS, No. 01-073-1592) as shown in Fig. 2a. When the

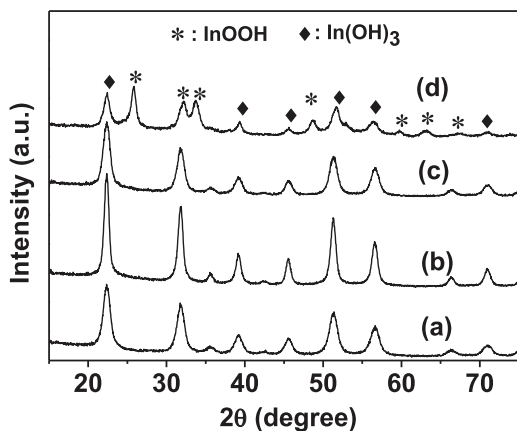


Fig. 2. The XRD patterns of the products obtained after different solvothermal time: (a) 1 h, (b) 3 h, (c) 6 h, and (d) 16 h.

solvothermal time was prolonged to 3 h, some irregular mesoporous architectures composed of pure $\text{In}(\text{OH})_3$ were observed (Figs. 1b and 2b). Observable small pores of ~ 6 nm clearly were associated with interlocking of the primary nanoplates. As the solvothermal time was extended to 6 h, the network-like architectures were formed (Fig. 1c), and much more pores were generated simultaneously. No obvious changes were observed from the XRD pattern (Fig. 2c). When the solvothermal time was increased to 16 h, the products shown in Fig. 1d were regular nanoporous nanospheres. The as-synthesized NPNSs were further observed with FESEM. Fig. 3a shows a low-magnification FESEM image of the as-synthesized precursor, which indicates that the sample was composed of a large quantity of well-dispersed spherical nanoparticles with a uniform diameter of about 100 nm. And the high-magnification image shown in Fig. 3b indicates that the nanosphere was built of numerous nanoplates, which connected each other and thus a nanoporous structure formed. Each nanoplate showed an edge length of about 8–15 nm and a thin thickness of about 2 nm. The corresponding XRD pattern (Fig. 2d) shows that the as-synthesized NPNSs were a mixture of $\text{In}(\text{OH})_3$ (JCPDS, No. 01-073-1592) and InOOH (JCPDS, No. 01-076-1552). And the broadened diffraction peaks further prove the small size of nanoplate-constructed NPNSs.

Based on the above results, a self-assembly mechanism for the precursor NPNS was summarized in Fig. 4. It was reported that the proportion of water played a key role in determining the crystal phase of hydrolysis product of InCl_3 in ethylenediamine–water system, i.e. $\text{In}(\text{OH})_3$ formed at high water proportion, while $\text{In}(\text{OH})_3$ dehydrated to InOOH when the water proportion was lowered. In the present ethanol–ethylenediamine system, In^{3+} ions were first hydrolyzed to form $\text{In}(\text{OH})_3$ due to the presence of water, which was mainly from the crystal water of $\text{In}(\text{NO}_3)_3 \cdot 4.5\text{H}_2\text{O}$. And

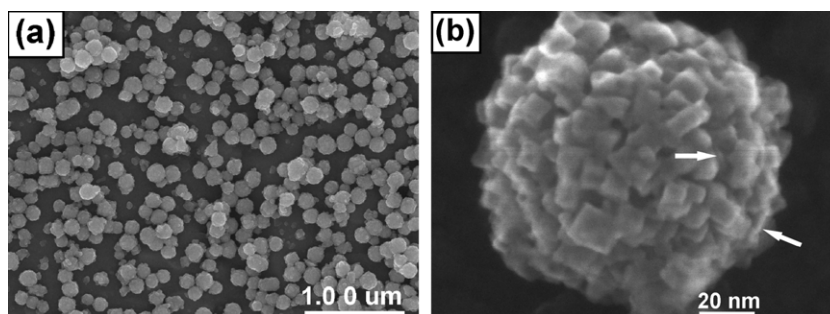


Fig. 3. (a) Low- and (b) high-magnification FESEM images of NPNSs precursor.

then some of $\text{In}(\text{OH})_3$ dehydrated to InOOH with increase of solvothermal reaction time. As for the morphology evolution, it was reported that $\text{In}(\text{OH})_3$ nanorod can be fabricated from $\text{In}(\text{OH})_3$ nanocubes via an induced anisotropic growth procedure, in which polyvinylpyrrolidone (PVP) was used as a directing agent [39,40]. Similarly, ethylenediamine, a capping agent with two basic functional groups ($-\text{NH}_2$), may coordinate to the lateral surfaces of $\text{In}(\text{OH})_3$ nanocrystals and result in a preferential growth or being assembled along certain directions. In the present solvothermal synthesis system, the excessive ethylenediamine may completely cover the $\text{In}(\text{OH})_3$ nanoplates, leading to the homogeneous interactions among the nanoplates, which facilitate the stacking of nanoplates. Finally, as shown in Fig. 4, $\text{In}(\text{OH})_3$ – InOOH nanoporous nanospheres are formed to minimize the surface energy [41].

3.2. Characterization of In_2O_3 NPNS

In_2O_3 NPNSs were obtained by calcining the precursor NPNSs at 500°C for 2 h in air. The TEM images in Fig. 5a and FESEM image in Fig. 5b indicate that In_2O_3 NPNSs basically remain the same morphology and architecture as its precursor. However, their size shrank slightly, which can be attributed to dehydration of precursors during the calcination process. Moreover, the ring-like SAED pattern (inset of Fig. 5a) indicates a polycrystalline structure of obtained In_2O_3 NPNSs, and the presence of obvious discrete spots suggests that the materials were well crystallized. The high-magnification TEM image in Fig. 5c shows In_2O_3 NPNSs were constructed by the interlocking stack of ultrathin nanoplates and confirms the single crystalline property of each nanoplate. The TEM image in Fig. 5c also reveals that the plate-like nanoparticles are irregular polygon with size of about 5–12 nm. The SEM image of commercial In_2O_3 nanocrystals (NCs) is also presented in Fig. 5d. The diameters of most commercial In_2O_3 nanoparticles were in the range of 40–90 nm. The XRD patterns (Fig. 5e) indicate that the In_2O_3 NPNSs were pure cubic phase (JCPDS, No. 06-0416), and the peaks of the In_2O_3 NPNSs were much weaker and broader than those of In_2O_3 NCs, which further confirms the smaller size of building blocks of NPNSs.

Brunauer–Emmett–Teller (BET) gas sorptometry measurements were conducted to examine the porous nature of the In_2O_3 NPNSs. Fig. 6 shows the N_2 adsorption/desorption isotherm and the pore-size distribution (inset of Fig. 6) of In_2O_3 NPNSs. The isotherms were identified as type IV, which is characteristic of mesoporous materials. The pore-size distribution obtained from the isotherm indicates the existence of a number of ~ 6 nm pores, which presumably arose

from the stacks of nanoplates. The larger pores of ~ 16 nm were attributed to the spaces among different NPNSs. The BET specific surface area of the sample calculated by the Barret–Joyner–Halenda (BJH) method was as high as $39.0\text{ m}^2\text{ g}^{-1}$, while that of commercial In_2O_3 NCs (Fig. 5d) was only $12.7\text{ m}^2\text{ g}^{-1}$. The BET specific surface area of TiO_2 (P25) was $\sim 50\text{ m}^2\text{ g}^{-1}$. The difference of the BET surface area between In_2O_3 NPNSs and In_2O_3 NCs can be attributed to the fact that the former have nanoporous architecture. In addition, the BET specific surface area of In_2O_3 NPNSs synthesized in the ethylenediamine–ethanol system was higher than that of In_2O_3 microsphere synthesized in the ethylenediamine–water system [42].

The UV–vis absorption spectra of In_2O_3 NPNSs, In_2O_3 NCs and P25 TiO_2 are shown in Fig. 7. The absorption of In_2O_3 NPNSs showed a slight blue-shift compared with those of In_2O_3 NCs. In_2O_3 has a small Bohr exciton radius of 2.14 nm. And the as-synthesized In_2O_3 NPNSs consisted of nanoplates with the thickness of about 2 nm, which is slightly smaller than the Bohr exciton radius (2.14 nm). Therefore, the slight blue-shift of UV–vis absorption may result from the quantum confinement effect.

3.3. Photocatalytic decomposition of PFOA

Comparative experiments were conducted to investigate the photocatalytic activity of In_2O_3 NPNSs, In_2O_3 NCs and TiO_2 for PFOA decomposition. The initial PFOA concentration was set at 30 mg L^{-1} . PFOA concentration on the order of mg L^{-1} has been measured in the receiving waters near specific point sources and in some industrial wastewater [43,44]. The initial pH value of PFOA solution after addition of 0.5 g L^{-1} In_2O_3 NPNSs was about 3.9. And no extra acid or base was added to adjust the pH value. The performances of these three catalysts for PFOA decomposition and defluorination are shown in Fig. 8. It is well known that direct photolysis of PFOA by 254 nm UV light is very slow and it was negligible in our experiments. As shown in Fig. 8a, PFOA was completely decomposed within 30 min in the presence of In_2O_3 NPNSs, while it decomposed less than 80% within 3 h by In_2O_3 NCs, and the decomposition rate was much slower by TiO_2 . Formations of fluoride ions during PFOA decomposition were monitored by IC, and the time-dependent defluorination of PFOA by different photocatalysts are shown in Fig. 8b. The defluorination ratio of PFOA by In_2O_3 NPNSs, In_2O_3 NCs and TiO_2 reached 71.0%, 29.7% and 5.1% after 3 h, respectively. These results clearly demonstrate that In_2O_3 NPNSs are much more active for PFOA decomposition than In_2O_3 NCs, which can be attributed to larger specific surface area and nanoporous structure of In_2O_3

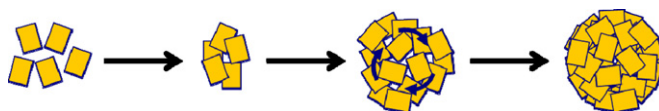


Fig. 4. Schematic illustration of NPNS formation via an interlocking stack.

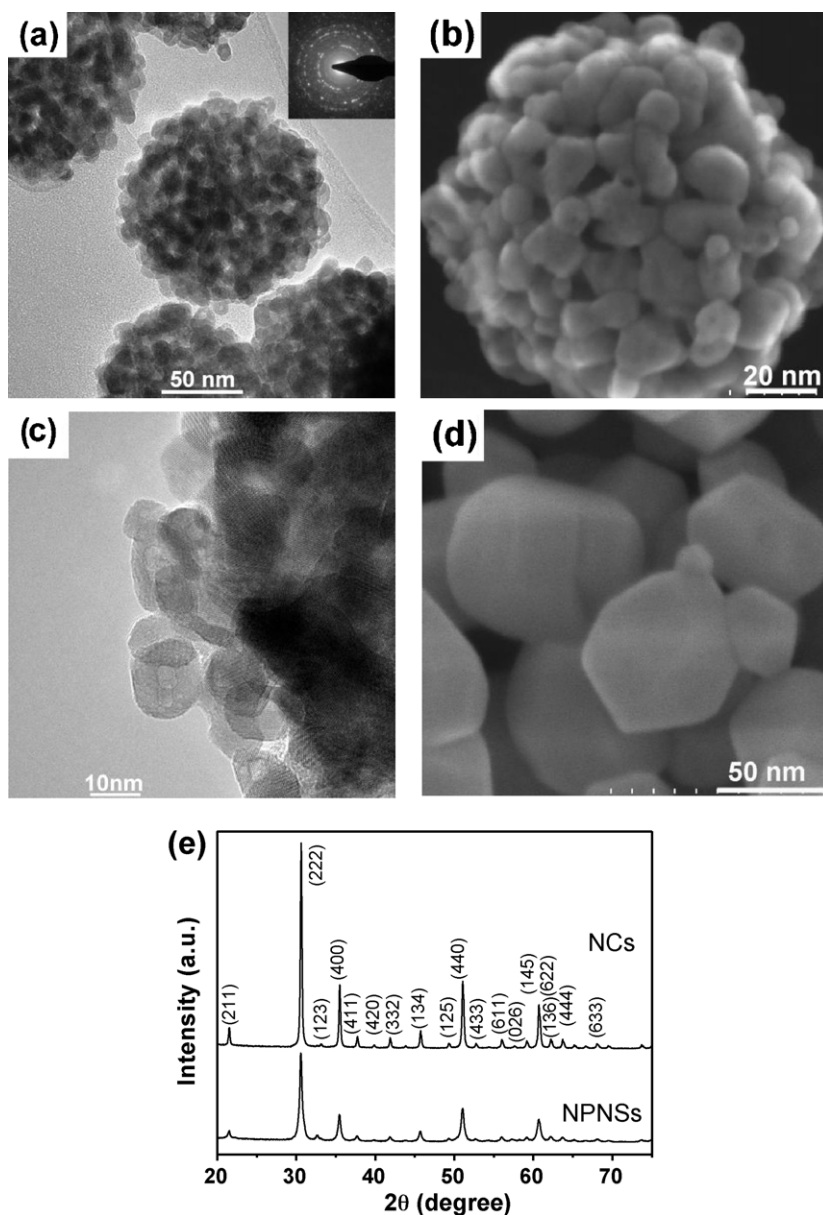


Fig. 5. (a) Low-magnification TEM images, (b) FESEM image, and (c) high-magnification image of In_2O_3 NPNSs, (d) FESEM image of commercial In_2O_3 nanocrystals (NCs), (e) XRD patterns of In_2O_3 NPNSs and NCs. The inset of (a) is SAED pattern.

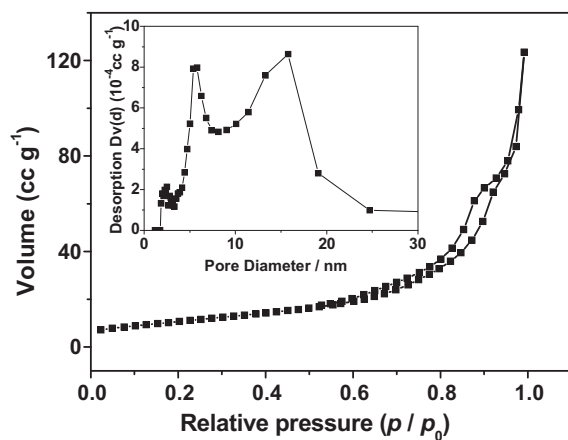


Fig. 6. Nitrogen adsorption–desorption isotherm of In_2O_3 NPNSs. The inset is (BJH) pore size distribution plot.

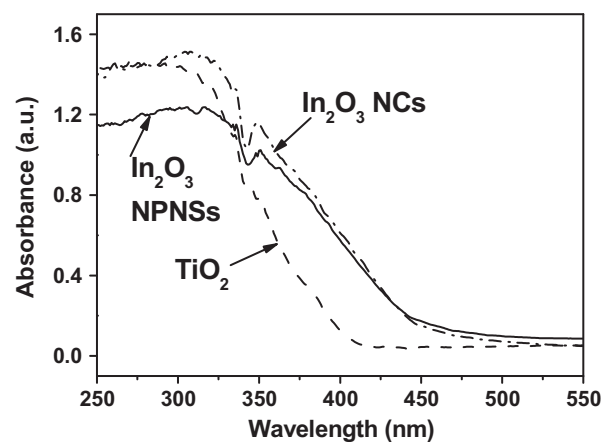


Fig. 7. UV–vis absorption spectra of In_2O_3 NCs, In_2O_3 NPNSs and TiO_2 .

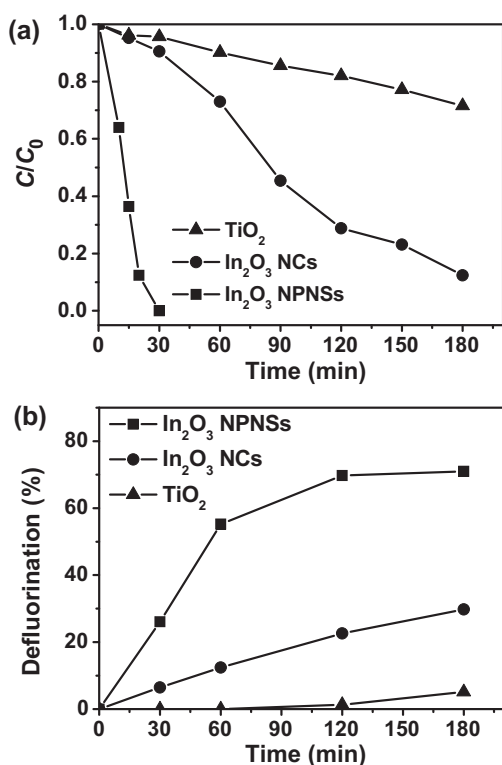


Fig. 8. (a) Photocatalytic decomposition of PFOA and (b) defluorination by In_2O_3 NPNSs, In_2O_3 NCs and TiO_2 .

NPNSs. Large surface area can offer more adsorption and reaction sites and accordingly has a beneficial effect on the activity of photocatalyst. The adsorption percentages of PFOA in the dark on In_2O_3 NPNSs, In_2O_3 NCs and TiO_2 were 27.4%, 19.4% and 2.23%, respectively. The nanoporous structure is beneficial for the diffusion of reactants and intermediates during reaction, which is one of important steps determining the reaction rate. Besides, the nano-size of ultrathin plates constructing In_2O_3 NPNSs shortens the diffusion distance of photogenerated carriers and reduces recombination of electron-hole pairs [45], which accordingly favors the photocatalysis of PFOA. All these factors make In_2O_3 NPNSs show much higher performance than In_2O_3 NCs.

The PFOA decomposition appears to follow pseudo first-order kinetics. The reaction rate constants (k) and half-life of PFOA ($\tau_{1/2}$) by different photocatalysts are listed in Table 1. The rate constant of In_2O_3 NPNSs was 5.89 h^{-1} , which was nearly 9 and 54.6 times higher than that of In_2O_3 NCs and TiO_2 respectively. The PFOA half-life during In_2O_3 NPNSs photocatalysis was as short as 7.1 min. And the corresponding energy consumption (it was defined as energy required to reduce PFOA to half of its initial concentration [16]) was $2.7 \text{ kJ } \mu\text{mol}^{-1}$ PFOA. Compared with other previously reported methods such as sonolysis, vacuum UV photolysis and UV persulfate, photocatalysis with In_2O_3 NPNS shows the highest reaction rate and relatively low energy consumption [16]. For example, sonolysis has the shortest half-life in the existing methods, which was 15 min for 200 nmol L^{-1} and 39 min for $20 \text{ } \mu\text{mol L}^{-1}$ PFOA,

Table 1
Reaction rate constants and half-life of PFOA decomposition by using different photocatalysts.

Photocatalyst	$k \text{ (h}^{-1}\text{)}$	$\tau_{1/2} \text{ (min)}$
In_2O_3 NPNSs	5.89	7.1
In_2O_3 NCs	0.66	63.0
P25 TiO_2	0.11	389.4

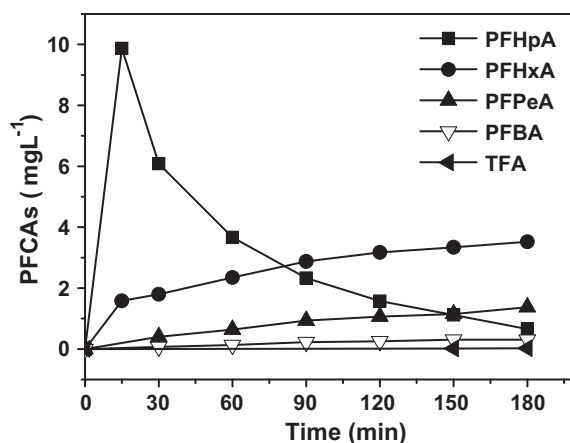


Fig. 9. Time-dependent change of intermediates during PFOA decomposition by using In_2O_3 NPNSs.

while the corresponding energy consumption was $1300 \text{ kJ } \mu\text{mol}^{-1}$ and $67 \text{ kJ } \mu\text{mol}^{-1}$ PFOA respectively.

3.4. Intermediates and decomposition mechanism

Intermediates during PFOA decomposition were identified and quantified with UPLC-MS/MS. And the main intermediates were shorter-chain PFCAs, i.e. perfluoroheptanoic acid (PFHpA, $\text{C}_6\text{F}_{13}\text{COOH}$), perfluorohexanoic acid (PFHxA, $\text{C}_5\text{F}_{11}\text{COOH}$), perfluoropentanoic acid (PFPeA, $\text{C}_4\text{F}_9\text{COOH}$), perfluorobutanoic acid (PFBA, $\text{C}_3\text{F}_7\text{COOH}$), and trifluoroacetic acid (TFA, CF_3COOH). Fig. 9 shows the time-dependent change of intermediates during PFOA decomposition by In_2O_3 NPNSs. PFHpA increased sharply to the maximum concentration of about 10 mg L^{-1} within 15 min and then decreased. And the amount of other intermediates continuously increased during 3 h reaction course. However none of their highest concentrations was over 4 mg L^{-1} . These observations suggest that photocatalytic decomposition of PFOA proceed in a step-by-step mode, i.e. one CF_2 unit is removed in one step. A scheme illustrating the decomposition of PFCAs is shown in Fig. 10, in which $\text{F}(\text{CF}_2)_n\text{COOH}$ represents PFOA and its main intermediates, i.e. shorter-chain PFCAs. The photocatalytic decomposition mechanism of PFCAs by TiO_2 has been proposed by Dillert et al. [17]. They suggested that the decomposition is initiated by a Kolbe-like

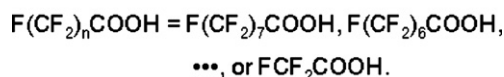
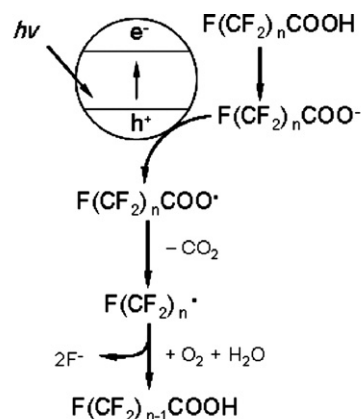


Fig. 10. Schematic illustration of PFCAs decomposition by In_2O_3 under UV irradiation.

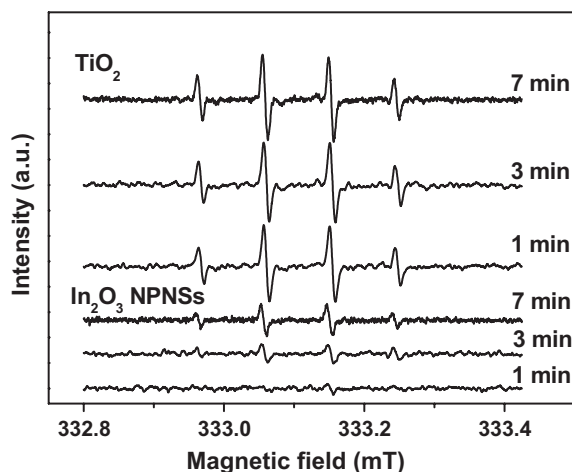


Fig. 11. ESR spectra of DMPO- OH^\bullet adduct under UV irradiation in the presence of In_2O_3 NPNSs or TiO_2 .

decarboxylation of PFOA to form a perfluoroalkyl radical. This step involves the electron transfer from the adsorbed perfluorocarboxylate anion to the valence band of the photocatalyst, where holes are generated by UV irradiation. Then, the terminal carboxylate group is cleaved, and perfluoroalkyl radical ($\text{C}_n\text{F}_{2n+1}^\bullet$) and CO_2 are accordingly formed. The perfluoroalkyl radical reacts with oxygen to form peroxy radical, which is further converted into PFOA with one less CF_2 unit and generates two fluoride ions.

To understand the origin of difference in the photocatalytic activity for PFOA decomposition between In_2O_3 and TiO_2 , formation of hydroxyl radicals (OH^\bullet) during PFOA decomposition in the presence of In_2O_3 NPNSs or TiO_2 under UV irradiation were monitored with ESR by using DMPO as the spin-trap agent, and the results are shown in Fig. 11. Four characteristic peaks of DMPO- OH^\bullet adduct with intensity ratio 1:2:2:1 were clearly recorded either in TiO_2 or In_2O_3 suspension, which indicates that photogenerated holes react with surface-bound water and/or hydroxide (OH^-) to form OH^\bullet even in the presence of PFOA. However, the DMPO- OH^\bullet signal in the case of TiO_2 were much higher than that in the case of In_2O_3 NPNSs, which indicates that more photogenerated holes are transformed into hydroxyl radicals in the case of TiO_2 than in the case of In_2O_3 . In addition, the intensity of DMPO- OH^\bullet signal hardly changed with illumination time when TiO_2 was used as photocatalyst, while it gradually increased when In_2O_3 NPNSs were used as photocatalyst. These results indicate that the photogenerated holes in TiO_2 preferentially react with water or hydroxide to form hydroxyl radicals, while those in In_2O_3 NPNSs tend to first react with PFOA. This difference can be attributed to the different adsorbability for PFOA by In_2O_3 NPNSs and TiO_2 , which is dependent on the surface properties [17]. High adsorbability for PFOA of In_2O_3 favors the direct electron transfer from PFOA to the valence band of In_2O_3 . Hydroxyl radical has been known to decompose a wide range of organic compounds through an H-atom abstraction to form water. However, in the case of PFOA, all hydrogen atoms have been replaced by fluorine atoms in the carbon chain, thus PFOA is inert to OH^\bullet attack ($k_{\text{OH}^\bullet + \text{PFOA}} \leq 10^5 \text{ M}^{-1} \text{ s}^{-1}$) [16,46]. In addition, perfluorination also reduces electron density of $-\text{COO}^-$ group in PFOA, thus the direct electron transfer from $-\text{COO}^-$ group in PFOA to HO^\bullet is unfavorable. In other words, the photogenerated holes in TiO_2 are preferentially transformed into hydroxyl radicals, which cannot effectively react with PFOA, while holes in In_2O_3 are less transformed into hydroxyl radicals and tend to react with PFOA directly. As a result, In_2O_3 NPNSs show much better photocatalytic activity for PFOA decomposition than TiO_2 .

4. Conclusion

In_2O_3 nanoporous nanospheres (NPNSs) with uniform size at $\sim 100 \text{ nm}$ were synthesized by a facile solvothermal method followed by calcination. The precursor of In_2O_3 NPNSs was self-assembled from ultrathin nanoplates in the ethylenediamine-ethanol solvothermal system. The as-synthesized In_2O_3 NPNSs possessed high specific surface area ($39.0 \text{ m}^2 \text{ g}^{-1}$) and a large number of nanopores at $\sim 6 \text{ nm}$. Compared with commercial In_2O_3 nanocrystals and TiO_2 , In_2O_3 NPNSs exhibit a remarkable photocatalytic activity for PFOA decomposition under mild conditions, which can be attributed to its nanostructure and the direct reaction between its photo-generated hole and PFOA. In addition, the In_2O_3 NPNSs-based photocatalysis has great advantages over existing methods for PFOA decomposition according to their reaction rate and energy consumption.

Acknowledgments

This work was supported by National Natural Science Foundation of China (21177071), Tsinghua University Initiative Scientific Research Program and China Postdoctoral Science Foundation (023207033).

References

- [1] P. Weihe, K. Kato, A.M. Calafat, F. Nielsen, A.A. Wanigatunga, L.L. Needham, P. Grandjean, *Environmental Science and Technology* 42 (2008) 6291.
- [2] G.B. Post, J.B. Louis, K.R. Cooper, B.J. Boros-Russo, R.L. Lippincott, *Environmental Science and Technology* 43 (2009) 4547.
- [3] J.P. Benskin, L.Y. Yeung, N. Yamashita, S. Taniyasu, P.K.S. Lam, J.W. Martin, *Environmental Science and Technology* 44 (2010) 9049.
- [4] J. Ho Yang, *Chemosphere* 8 (2010) 548.
- [5] G.P. Zhao, J. Wang, X.F. Wang, S.P. Chen, Y. Zhao, F. Gu, A. Xu, L.J. Wu, *Environmental Science and Technology* 45 (2011) 1638.
- [6] T.J. Wallington, M.D. Hurley, J. Xia, D.J. Wuebbles, S. Sillman, A. Ito, J.E. Penner, D.A. Ellis, J. Martin, S.A. Mabury, O.J. Nielsen, M.P. Sulbaek Andersen, *Environmental Science and Technology* 40 (2006) 924.
- [7] E. Sinclair, K. Kannan, *Environmental Science and Technology* 40 (2006) 1408.
- [8] M.M. Schultz, C.P. Higgins, C.A. Huset, R.G. Luthy, D.F. Barofsky, J.A. Field, *Environmental Science and Technology* 40 (2006) 7350.
- [9] H. Moriwaki, Y. Takagi, M. Tanaka, K. Tsuruho, K. Okitsu, Y. Maeda, *Environmental Science and Technology* 39 (2005) 3388.
- [10] C.D. Vecitis, H. Park, J. Cheng, B.T. Mader, M.R. Hoffmann, *Journal of Physical Chemistry A* 112 (2008) 4261.
- [11] H. Park, C.D. Vecitis, J. Cheng, W.Y. Choi, B.T. Mader, M.R. Hoffmann, *Journal of Physical Chemistry A* 113 (2009) 690.
- [12] J. Chen, P. Zhang, *Water Science and Technology* 54 (2006) 317.
- [13] H. Hori, A. Yamamoto, E. Hayakawa, S. Taniyasu, N. Yamashita, S. Kutsuna, H. Kiatagawa, R. Arakawa, *Environmental Science and Technology* 39 (2005) 2383.
- [14] H. Hori, E. Hayakawa, H. Einaga, S. Kutsuna, K. Koike, T. Ibusuki, H. Kiatagawa, R. Arakawa, *Environmental Science and Technology* 38 (2004) 6118.
- [15] H. Hori, E. Hayakawa, K. Koike, H. Einaga, T. Ibusuki, *Journal of Molecular Catalysis A: Chemical* 211 (2004) 35.
- [16] C.D. Vecitis, H. Park, J. Cheng, B.T. Mader, M.R. Hoffmann, *Frontiers of Environmental Science & Engineering in China* 3 (2009) 129.
- [17] R. Dillert, D. Bahnemann, H. Hidaka, *Chemosphere* 67 (2007) 785.
- [18] S.C. Panchangam, A.Y. Lin, K.L. Shaik, C. Lin, *Chemosphere* 77 (2009) 242.
- [19] S.C. Panchangam, A.Y. Lin, J. Tsai, C. Lin, *Chemosphere* 75 (2009) 654.
- [20] Y. Chen, S. Lo, J. Kuo, *Water Research* 45 (2011) 4131.
- [21] F. Quarto, C. Sunseri, S. Piazza, M. Romano, *Journal of Physical Chemistry B* 101 (1997) 2519.
- [22] I. Hamburg, C.G. Granqvist, *Journal of Applied Physics* 60 (1986) 123.
- [23] X. Li, M.W. Wanlass, T.A. Gessert, K.A. Emery, T. Coutts, *Journal of Applied Physics Letters* 54 (1989) 2674.
- [24] D.G. Shchukin, J.H. Schattka, M. Antonietti, R.A. Caruso, *Journal of Physical Chemistry B* 107 (2003) 952.
- [25] J. Lv, T. Kako, Z. Li, Z. Zou, J. Ye, *Journal of Physical Chemistry C* 114 (2010) 6157.
- [26] J. Mu, B. Chen, M. Zhang, Z. Guo, P. Zhang, Z. Zhang, Y. Sun, C. Shao, Y. Liu, *ACS Applied Materials & Interfaces* 4 (2012) 424.
- [27] D. Wang, Z. Zou, J. Ye, *Chemistry of Materials* 17 (2005) 3255.
- [28] K.R. Reyes-Gil, E.A. Reyes-García, D. Raftery, *Journal of Physical Chemistry C* 111 (2007) 14579.
- [29] N. Arai, N. Saito, H. Nishiyama, Y. Shimodaira, H. Kobayashi, Y. Inoue, K. Sato, *Journal of Physical Chemistry C* 112 (2008) 5000.
- [30] N. Bao, L. Shen, T. Takata, K. Domen, *Chemistry of Materials* 20 (2008) 110.

- [31] J.S. Hu, L.L. Ren, Y.G. Guo, H.P. Liang, A.M. Cao, L.J. Wan, C.L. Bai, *Angewandte Chemie International Edition* 44 (2005) 1269.
- [32] G.L. Drisko, V. Luca, E. Sizgek, N. Scales, R.A. Caruso, *Langmuir* 25 (2009) 5286.
- [33] L.Y. Chen, T. Fujita, Y. Ding, M.W. Chen, *Advanced Functional Materials* 20 (2010) 2279.
- [34] J. Hu, L. Ren, Y. Guo, H. Liang, A. Cao, L. Wan, C. Bai, *Angewandte Chemie International Edition* 44 (2005) 1269.
- [35] Y. Li, G. Chen, Q. Wang, X. Wang, A. Zhou, Z. Shen, *Advanced Functional Materials* 20 (2010) 3390.
- [36] Y.W. Zhang, R. Si, C.S. Liao, C.H. Yan, C.X. Xiao, Y. Kou, *Journal of Physical Chemistry B* 107 (2003) 10159.
- [37] J.P. Cheng, X.B. Zhang, X.Y. Tao, H.M. Lu, Z.Q. Luo, F. Liu, *Journal of Physical Chemistry B* 110 (2006) 10348.
- [38] L. Chen, X. Yang, J. Chen, J. Liu, H. Wu, H. Zhan, C. Liang, M. Wu, *Inorganic Chemistry* 49 (2010) 8411.
- [39] J. Huang, L. Gao, *Crystal Growth and Design* 6 (2006) 1528.
- [40] T. Tseng, W.J. Tseng, *Ceramics International* 35 (2009) 2837.
- [41] D.F. Zhang, L.D. Sun, J.L. Yin, C.H. Yan, *Advanced Materials* 15 (2003) 1022.
- [42] X. Wang, M. Zhang, J. Liu, T. Luo, Y. Qian, *Sensors and Actuators B: Chemical* 137 (2009) 103.
- [43] C.A. Moody, J.A. Field, *Environmental Science and Technology* 33 (1999) 2800–2806.
- [44] A.Y. Lin, S.C. Panchangam, C. Lo, *Environmental Pollution* 157 (2009) 1365–1372.
- [45] Z. Zhang, C.C. Wang, R. Zakaria, J.Y. Ying, *Journal of Physical Chemistry B* 102 (1998) 10871.
- [46] S. Kutsuna, Y. Nagaoka, K. Takeuchi, H. Hori, *Environmental Science and Technology* 40 (2006) 6824–6829.